Adaptive Optics pre-compensated laser uplink to LEO and GEO

JAMES OSBORN,[1,*] **MATTHEW J. TOWNSON,**[1] **OLLIE J. D. FARLEY,**[1] **ANDREW REEVES,**[2] **AND RAMON MATA CALVO**[2]

[1]*Durham University, Dept. Physics, Lower Mountjoy, South Rd, Durham DH1 3LE, UK*
[2]*German Aerospace Center, Münchnerstrasse 20, 82234 Wessling, Germany*
[*]*james.osborn@durham.ac.uk*

Abstract: We present the results from a Monte Carlo computer simulation of adaptive optics (AO) pre-compensated laser uplink propagation through the Earth's atmospheric turbulence from the ground to orbiting satellites. The simulation includes the so-called point-ahead angle and tests several potential AO mitigation modes such as tip/tilt or full AO from the downlink beam, and a laser guide star at the point ahead angle. The performance of these modes, as measured by metrics relevant for free-space optical communication, are compared with no correction and perfect correction. The aim of the study is to investigate fundamental limitations of free-space optical communications with AO pre-compensation and a point-ahead angle, therefore the results represent an upper bound of AO corrected performance, demonstrating the potential of pre-compensation technology. Performance is assessed with varying launch aperture size, wavelength, launch geometry, ground layer turbulence strength (i.e. day/night), elevation angle and satellite orbit (Low-Earth and Geostationary). By exploring this large parameter space we are able examine trends on performance with the aim of informing the design of future optical ground stations and demonstrating and quantifying the potential upper bounds of adaptive optics performance in free-space optical communications.

1. Introduction

Laser propagation between the ground and space is used for free space optical communications (FSOC) [1,2] to securely transfer data at high-data rates. Information is exchanged between the satellite and the ground via laser beams rather than more traditional radio frequencies. This light-weight and low-power alternative [1] is also considered more secure due to the line of sight nature and small divergence and has the potential of higher data bandwidths [2]. Additionally FSOC can support quantum key distribution (QKD) [3,4] schemes. However, the stability and performance of FSOC can be fundamentally limited by the turbulence in the Earth's atmosphere. This turbulence leads to beam spread that reduces the intensity received at the target and; "jitter", or beam wander, and "scintillation", where the beam splits into many speckles, which both introduce a variation in the received signal. In FSOC the fluctuations in received intensity due to the atmospheric channel lead to fade and surge events increasing the Bit-Error-Rate (BER) and significantly limiting the achievable bandwidth [5]. Both of these phenomena can be mitigated with adaptive optics (AO) systems that can be used to pre-compensate the laser beam to correct for the detrimental effects of the atmospheric channel (see for example [6–9]).

For the AO system to operate, the atmosphere must be probed to measure the distortion imposed by the atmospheric turbulence. For FSOC, this can be achieved by using the downlink beam from the satellite itself as a guide source. Otherwise, reflected light from the object could be used if the return intensity is high enough. Due to the apparent motion of the satellite in the sky and the light travel time, the uplink laser must be transmitted to a point in front of the current observed position of the satellite such that the satellite receives the signal, this angle is known as the "point-ahead angle". In this case the measurements of the atmospheric turbulence from

the satellite downlink can be decorrelated from the atmospheric turbulence the uplink beam propagates through, leading to reduced performance.

Here we explore the effect of atmospheric turbulence on laser beams propagating to space, to both low earth orbit (LEO) and geostationary orbit (GEO). We include the impact of introducing AO pre-compensation to the uplink beam and the effects of the point-ahead angle on the correction. We have chosen the main metrics to present to be the distributions of fraction of power received at the satellite relative to the power of the launched beam and the variance of the received signal. These results can be processed further to calculate the expected BER and fade statistics for an FSOC link, with an example of this shown later in the paper, but this work is also relevant to other applications, for example laser ranging.

We use a Monte-Carlo simulation to model the system with an idealised AO model to demonstrate the full potential of AO links without AO system effects such as temporal or fitting errors or assessing the technical feasibility. From these results we create an envelope showing the maximal performance that could be achieved for each of the AO regimes in various conditions rather than choosing a particular set of system parameters to generate a realistic performance for one specific case.

Due to the nature of atmospheric turbulence, the performance of laser propagation systems are strongly dependent on the transmitter aperture size. Therefore, we assess the effect of varying the transmitter aperture size with various AO mitigation techniques. There are currently no analytical models for partial uplink AO pre-compensation that include diffractive effects and the propagation of the wavefront. This is the first study to assess and present the potential gains over a wide range of situations in order to understand the trends in performance. We aim to determine if AO can enable larger launch apertures, effectively reducing the geometric beam divergence whist mitigating the effects of the turbulence. The result is higher signal-to-noise ratios (and hence lower BER) at the satellite and lower variance (lower probability of fade). This may be required for high-bandwidth or QKD applications.

We consider links with different wavelengths, launch beam shapes (Gaussian or Bessel-Gauss), turbulence strength (day or night), elevation angle and propagation distance (LEO and GEO).

In section 2 we present the parameters space used in this study. Sections 3 and 4 describe the simulation and atmospheric model used. Section 5 describes the various AO modes under investigation and section 6 presents the metrics used to analyse the results. Finally the results, discussion and conclusions of the study are shown in sections 7, 8 and 9.

2. System configurations

Table 1 shows the system parameters used for this study with the symbols used to represent them. The parameters have been chosen to be representative of realistic laser propagation systems [2,10–12].

Table 1. System parameters used in this study.

Parameter	Value		Symbol
	LEO	GEO	
Propagation distance (m)	0.5×10^6	36×10^6	L
Point ahead angle ($''$)	10	3.7	θ_P
Wavelength (nm)	850, 1064, 1550	1550	λ
Receiver diameter (m)	0.05	0.25	D_{R_x}
Elevation angle (°)	10, 30, 90	30	θ_E
Transmitter beam radius (m)	Variable 0.02 – 0.25		R_{T_x}
Launch beam shape	Gaussian, Bessel-Gaussian		B

The transmitted beam radius is varied between 0.02 and 0.25 m. Although some systems will use smaller effective launch apertures than our minimum, we are concentrating in the effect of uplink correction on the beam. As will be seen, we do not expect uplink correction of smaller beams to offer much benefit, as the receiver-plane beam profile will be dominated by diffractive beam spreading due to the small size of the launch.

The laser beam is shaped in two different ways; a Gaussian beam and a Bessel-Gaussian beam. For small launch apertures it is feasible to use a refracting telescope as the transmitter, allowing a Gaussian beam to be used. For larger launch apertures reflecting telescopes are required. The secondary obscuration of most reflectors means that it is not possible to launch a Gaussian beam. In this case, the Gaussian beam must be launched from a sub-aperture of the main telescope. A novel idea to side-step this issue is to construct a Bessel-Gauss beam to launch around the secondary obscuration [9]. Here, we assess a Bessel-Gauss beam launch to assess its suitability for such scenarios.

For LEO we model wavelengths of 1550, 1064 and 850 nm. These wavelengths cover typical atmospheric windows. The latter wavelength can be used in potential QKD schemes [13], whereas the longer wavelengths can be used for more traditional optical communications that make use of existing telecommunications components [11].

For LEO we test elevation angles of 10, 30 and 90° with the aim of understanding how the performance scales with the varying elevation angles required to track a LEO object across the sky and to maximise the duration of the link. For GEO we only test 30° elevation angle as a representative value.

3. Simulation

We have developed an Monte-Carlo simulation for laser uplink experiments. The simulation includes a number of turbulent layers in the atmosphere, each defined by a strength and velocity (see section 4 for a description of the atmospheric model). These layers are made using the AOtools python package [14]. For each simulation run, we use 5000 independent atmosphere instances in order to ensure statistical convergence.

The simulation utilises Fresnel propagation between these layers on the uplink path. For the final step to the plane of the satellite, if the satellite is in the far-field ($L \gg 2R_{T_x}^2/\lambda$) (usually GEO) then the final propagation from the top of the atmosphere to the satellite is made with a Fraunhofer assumption rather than Fresnel [15].

The downlink and uplink paths can be separated in angle to replicate a point-ahead angle. This results in the beams becoming spatially separated at higher atmospheric turbulence layers.

The projected size of a simulated element, i.e. pixel, at the receiver-plane is usually around 20 cm depending on propagation distance and size of the launch aperture. The pixel scale in the receiver-plane is not fixed in the simulation. Instead we fix the number of pixels across the receiver-plane. As larger propagation distances or smaller launch apertures result in larger beam sizes, this also means that the pixel size is also larger. This does not impact the result as the pixel size is always small compared to the spatial correlation length of the beam intensity in the receiver-plane.

The modular nature of the simulation means that various mitigation techniques can be trialled. The AO modes tested here are explained further in section 5. The simulation can be run in 'ideal AO mode' with no latency and perfect wavefront correction (i.e. using the measured phase for the correction), or in a realistic mode where only a given number of Zernike modes are corrected and a correction latency can also be included. In this work we run the AO in 'ideal AO mode' to assess trends in performance due to the optical propagation and system geometry and to examine the full potential of these systems. Assessment of AO system parameters will follow in future work. In addition the AO wavefront sensor can sample either the downlink or uplink path in order to assess the effect of the point-ahead angle.

There are some limitations to the simulation. Cone effect, or focal anisoplanatism, is not included and so all AO beacons are assumed to be at infinite distance. This is an acceptable assumption here, where the ratio of the transmitter and receiver sizes to the propagation distance is very small, even at the largest end of our test range. This means that the focal anisoplanatism is negligible. The system only includes atmospheric turbulence and not local 'dome' turbulence; atmospheric attenuation, absorption or scattering; wind shake or tracking errors. Although each of these could be included, realistic values are not readily available. The largest limitation of the simulation is the atmospheric model used to represent the Earth's atmospheric optical turbulence. In reality the Earth's atmosphere is a dynamic environment with variations of turbulence strength and altitude on time scales of minutes to days [16–18]. The Earth's atmospheric optical turbulence generally consists of several turbulence zones or layers which vary in altitude and strength. The atmospheric models commonly used in studies do not reflect this structure or variability. Here, we comply with previous studies and implement the Hufnagel-Valley model [19] (see section 4.). Although not entirely realistic this model still enables us to study and compare various mitigation scenarios for factors such as wavelength, elevation angle, etc.

For the case of uncorrected propagation, the simulation results have been compared to the theoretical expression of [20]. The comparisons are shown in the figures throughout. Similar analytical expressions do not yet exist for partial AO correction.

4. Atmosphere

The Earth's atmospheric optical turbulence is highly variable, both spatially and temporally, however in order to effectively compare between different configurations we use a standard atmosphere, in this case the modified Hufnagel-Valley profile [19],

$$
\begin{aligned}
C_n^2(h) = {} & 5.94 \times 10^{-3} \left(\frac{w}{27}\right)^2 \left(\frac{h}{10^5}\right)^{10} \exp\left(-\frac{h}{1000}\right) \\
& + 2.7 \times 10^{-16} \exp\left(-\frac{h}{1500}\right) + A \exp\left(-\frac{h}{100}\right),
\end{aligned}
\tag{1}
$$

where h is the height in metres above ground level, w is the root-mean-square wind speed in m/s and A is a scaling factor for the ground-layer turbulence strength. For $A = 1.7 \times 10^{-14}$ m$^{-2/3}$ and $w = 21$ m/s the model reduces to the common HV-5/7 model, so called as the resultant coherence length, $r_0 = 5$ cm and the isoplanatic angle, θ_0, is 7 μradians. Here, we use two standard Hufnagel-Valley parameterisations, the weak case ($A = 1.7 \times 10^{-14}$ m$^{-2/3}$) and strong case ($A = 1.7 \times 10^{-13}$ m$^{-2/3}$). This corresponds to a spatial coherence length, of $r_0 = 5$ cm and $r_0 = 1.5$ cm respectively at 500 nm. The spatial coherence length is sometimes referred to as the 'Fried parameter'. The strong profile is more consistent with daytime operations where the ground layer turbulence tends to be much stronger due to the solar heating of the ground.

To facilitate comparison with previous work, we have chosen to use the Hufnagel-Valley model for the vertical distribution of optical turbulence. However, due to computational restrictions limiting the number of layers which can be simulated in a reasonable time frame, this model is sub-sampled to seven turbulent layers using the equivalent layers method [21], see Fig. 1. The turbulence strength is parameterised by the integrated turbulence within a vertical slab of thickness dh. Hence when we present the sub-sampled profile in Fig. 1 it appears that each layer is stronger than that modelled by the HV-5/7 profile, however the integrated turbulence strength is conserved.

However, i) in this study we concentrate on the effect of the point-ahead angle and potential mitigation techniques, for this reason, it is more important that our atmospheric model has an appropriate isoplanatic angle; ii) as the HV profile is not actually representative of any real instantaneous profile, small variations are inconsequential; and iii) we are interested in general
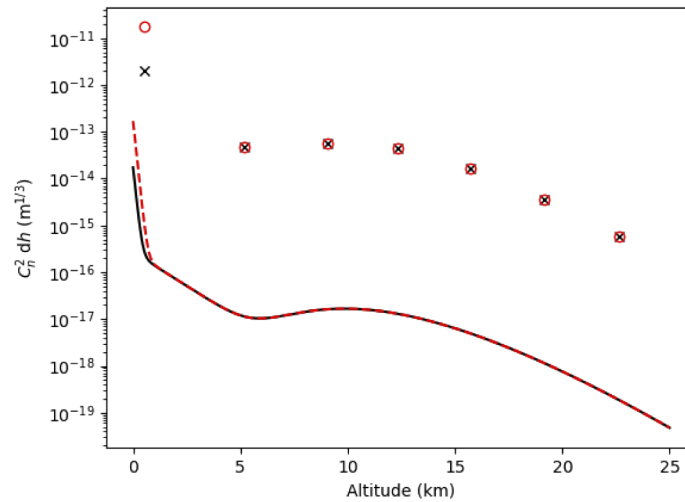
Fig. 1. Vertical distribution of the optical turbulence (lines) used in the simulations reduced to seven layers using the equivalent layers method (points). Black line and crosses indicate the weak turbulence case and red dashed line and open circles indicate the strong turbulence case.

trends of varying macro-parameters rather than absolute values which certainly vary depending on the exact instantaneous turbulence profile at the time of measurement.

The first layer of the compressed atmosphere is not at $h = 0$ m. This is an artefact of the equivalent layers method which aims to conserve isoplanatic angle and integrated turbulence strength. It is possible to force the ground layer to be at $h = 0$ m but it is more realistic to simulate the 'ground' layer slightly above the ground to emulate an extended ground layer.

The outer scale and inner scale are set to infinity and zero respectively. While it would be more accurate to include these parameters, measurements of realistic values is not available. Here we

Table 2. Vertical profile for the turbulent atmosphere used in this study. Note that only the first bin is different between the strong (daytime) and weak (night-time) model. We also show atmospheric parameters for the turbulent atmosphere used in this study. Note that all parameters are computed at a zenith.

Layer altitude (m)	C_n^2 HV-weak (m$^{-2/3}$)	C_n^2 HV-strong (m$^{-2/3}$)	
198	2.06e-12	1.73e-11	
5188	4.80e-14	4.80e-14	
9050	5.49e-14	5.49e-14	
12321	4.42e-14	4.42e-14	
15707	1.63e-14	1.63e-14	
19165	3.61e-15	3.61e-15	
22662	5.65e-16	5.65e-16	
Atmospheric Parameter at λ (nm)	500	1550	500	1550
Coherence length, r_0 (cm)	5.0	19.3	1.5	5.6
Isoplanatic angle, θ_0 (μ rad)	7.17	27.86	6.68	25.95
Downlink Rytov variance, σ_R^2	0.22	0.06	0.76	0.20

therefore decide to use Kolmogorov turbulence such that the results can easily be compared to other studies and analytical solutions.

Table 2 shows the vertical turbulence distribution and the integrated parameters at 500 nm and 1550 nm for the model used in this study .

5. Adaptive optics

AO is an attractive facility to optimise uplink propagation. If it is possible to perfectly correct for the atmospheric effects then the beam in the receiver plane will be shaped purely by diffraction from the aperture. This will result in a higher transmitted power and a connection with low variance, maximising the singal-to-noise ratio. However, AO correction requires a probe through the atmospheric channel in order to measure and ultimately correct for the deformations in the wavefront. For the case of laser uplink to satellites this is complicated by the point-ahead angle. Here, several options are assessed:

- No correction ('uncorrected').

- Use downlink beam to correct for tip/tilt of uplink ('TT_PA'). The Z-tilt across the launch aperture is calculated from the satellite beacon and subtracted from the launch wavefront.

- Use downlink beam to correct all spatial modes of uplink ('AO_PA'). The incoming wavefront itself is subtracted from the launch beam before the uplink propagation.

- Use a Laser Guide Star at the point-ahead angle to correct higher spatial orders of uplink. Tip/tilt/focus still from downlink beam ('LGS_PA'). In this case the tip/tilt and focus modes are fitted to the LGS wavefront and removed. The tip/tilt and focus modes are also fitted to the satellite beacon downlink and is then added to the LGS wavefront before projecting onto the deformable mirror.

- Perfect AO correction of uplink (for reference) ('AO'). In this case the wavefront in the direction of the satellite is directly applied as a pre-correction. Note that this does not include the geometric divergence of the uplink beam and so residual errors remain, but this is seen as the best case scenario.

The difference between 'AO_PA' and 'AO' demonstrates the effect of the anisoplanatism due to the point-ahead angle, whereas the difference between 'LGS_PA' and 'AO' demonstrates the effect of the point-ahead angle on tip/tilt and focus.

The AO modes are simulated in an idealised way. We do not consider realistic effects such as temporal or spatial sampling errors or fitting errors. We also do not consider the impact of the atmospheric propagation on the ability to reconstruct the wavefront, which is challenging in strong turbulence conditions. This study represents a best-case performance.

There are several complications associated with AO for beams propagating to satellites. For example, even ignoring the point-ahead angle, diffractive beam spread of the uplink beam between turbulent layers means that the downlink and uplink paths are not necessarily reciprocal, especially for small launch diameters which result in larger diffractive beam spread. The beam will sample larger volumes of higher-altitude turbulent zones than lower altitudes. this results in the turbulence appearing stronger, but also in the case that the downlink beam is used as a probe for AO correction, either full or tip/tilt only correction, these signals will be less correlated with the uplink - reducing the AO performance.

Similarly, the point-ahead angle of uplink connections to LEO or GEO, means that the downlink and uplink beams will be spatially separated at the altitude of the turbulence layers (above the surface layer). This separation leads to a decorrelation of the wavefront and limits

the performance of the AO system. In the extreme cases we expect low order AO systems to outperform higher-order correction systems as the higher-orders will decorrelate more quickly than the low orders, essentially adding noise to the correction.

Both of these effects will be amplified at lower elevation angles, where increased propagation path length through the turbulence atmosphere leads to larger diffractive beam spread and larger absolute difference in beam paths through the turbulence.

6. Metrics

The simulation provides a 2-dimensional map of electric-field at the receiver-plane, in this case the altitude of the satellite. Here we are interested in the received signal within a small receiver.

The sampling of the simulated receiver-plane has square resolution elements with a size similar to the diameter of the receiver. The size of these elements varies slightly depending on the propagation distance and size of the launch aperture, but is usually around 20 cm. We assume that the correlation length of the beam intensity in the receiver-plane is significantly larger than the receiver aperture size [20] and therefore the receiver aperture is entirely within a single simulated element. We calculate the received intensity by multiplying the single element intensity by the ratio of the area of the receiver telescope to the area of the element.

We have chosen three metrics to parameterise the effect of the atmospheric channel on the optical propagation:

- Long-term beam radius, W_{LT}. The long-term beam size is found from the $1/e^2$ radius of the simulated long-term intensity distribution in the pupil plane of the receiver.

- Mean received intensity as a fraction of total intensity in the receiver plane. This includes both beam divergence and beam wander.

- Received intensity variance normalised by the total intensity in the receiver plane (scintillation index).

- Probability of fade, where the signal drops below some threshold relative to the mean.

- Mean BER for direct detection (On-Off keying)

The probability of fade is calculated by integrating the probability density distribution (p_I) as a function of threshold level (I_T) [20],

$$P(I \leq I_T) = \int_0^{I_T} p_I(I)dI, \tag{2}$$

and the BER for on-off keying is calculated using,

$$\langle \mathrm{BER} \rangle = \frac{1}{2} \int_0^\infty p_I(I)\mathrm{erfc}\left(\frac{\langle \mathrm{SNR} \rangle I}{2\sqrt{2}\langle I \rangle}\right) dI, \tag{3}$$

where SNR is the signal-to-noise ratio, $\langle \rangle$ indicates the expected value and erfc is the complimentary error function. There are several models which can be used to describe the probability density function of the received intensity [22]. However, as we are using a simulation to provide the distribution of received intensity, we do not need to impose any particular distribution. Instead we use measured relative density of the received intensity to estimate the probability of fade and BER directly.

7. Results

All results presented here are for the weak turbulence case and at 30 degree elevation, unless stated otherwise. The integrated atmospheric parameters are shown in Table 3.

Instantaneous and long exposure beam images are shown in Fig. 2. As expected the smaller launch apertures lead to a larger diffractive beam spread and therefore a larger beam (both long and short exposure) in the receiver plane. This large beam size in comparison with the receiver aperture size (only one pixel in the image) means that the variance in received intensity is low when compared to larger launch apertures. In this case the effect of beam wander and scintillation are both negligible because the coherence length is so large, the received intensity is stable irrespective of any motion of the beam. This is counter to the downlink situation where larger receiver apertures act to average out the scintillation speckles.
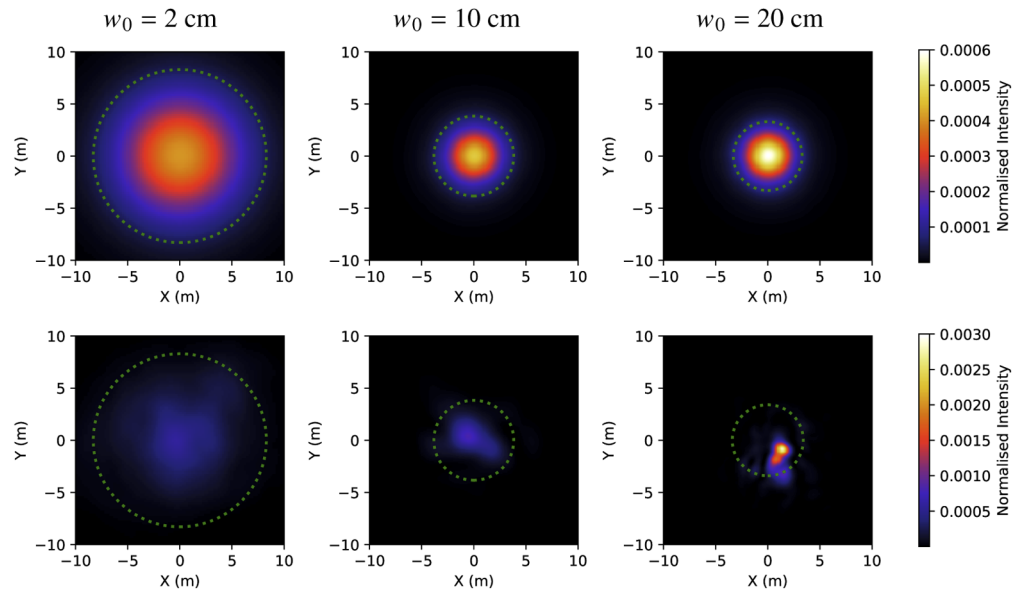

Fig. 2. Top row: Long-exposure images of beam at LEO for 0.02, 0.1 and 0.2 m Gaussian launch beam radius at 1064 nm and at 90 degrees elevation angle. Bottom row: Same but instantaneous beam image. Green circle indicates size of $1/e^2$ beam radius of long-exposure image (8.3, 3.8 and 3.3 m respectively). The integrated intensity in the receiver-plane is normalised to unity. In this figure the entrance pupil of the receiver spans one pixel.

Table 3. Integrated atmospheric parameters at 30 degree elevation.

Optical turbulence parameters	Weak turbulence 30 degrees	
λ (nm)	500	1550
Coherence length r_0 (cm)	3.3	12.8
Isoplanatic angle θ_0 (μ rad)	2.36	9.19
Downlink Rytov variance σ_R^2	0.796	0.213

Larger apertures would be preferable as the smaller beam size in the receiver plane leads to higher peak intensity, hence greater link efficiency. However, beam wander and scintillation lead to significant intensity variance and long duration fades. With AO correction beam wander and scintillation can be reduced, resulting in an uplink with high efficiency and stable received

intensity. Importantly, larger launch apertures, in combination with AO pre-compensation can lead to links with a higher received intensity, and hence a higher signal-to-noise ratio, and a lower variance (reduced fades).

7.1. AO correction modes

Figure 3 shows the relative density of the received intensity distributions for three example launch beam radii, 0.02, 0.1 and 0.2m. The relative density distribution combines the beam divergence, beam wander and scintillation components.
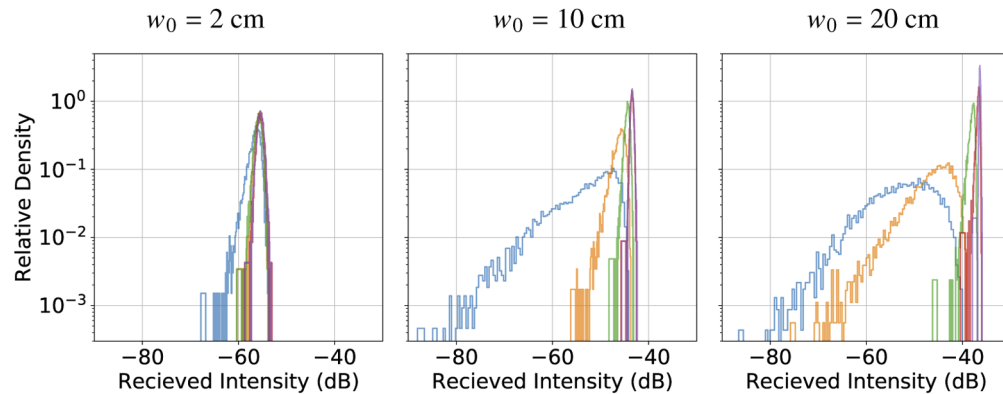

Fig. 3. Relative density of received intensity distribution for various adaptive mitigation for a 2 cm (left column) 10 cm (centre column) and 20 cm (right column) Gaussian launch beam radius and 1550 nm wavelength at 30 degrees elevation angle. The received intensity probability distribution is measured relative to the total intensity in the receiver-plane. The colour indicates the AO mode; blue is uncorrected; yellow is 'TT_PA'; green is 'AO_PA'; red is 'LGS_PA'; and purple is perfect 'AO'.

Figure 4 shows the beam metrics for the various AO mitigation scenarios as a function of $1/e^2$ launch beam radius.
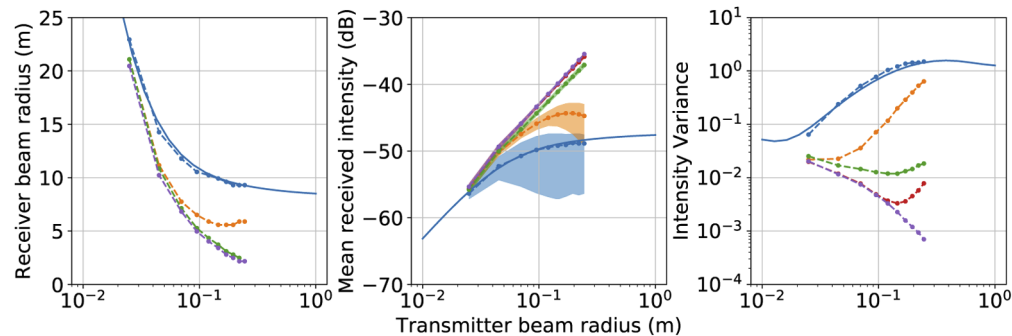

Fig. 4. Expected beam parameters with various correction techniques for an uplink optical propagation to LEO at 30 degrees elevation and at 1550 nm. From left to right, we show the receiver plane beam width, fractional received intensity and intensity variance. The solid lines indicate the theoretical values for an uncorrected, collimated, Gaussian beam. For the mean received intensity, the coloured region indicates the inter-quartile range of the distribution. The colour indicates the AO mode; blue is uncorrected; yellow is 'TT_PA'; green is 'AO_PA'; red is 'LGS_PA'; and purple is perfect 'AO'.

As expected, for larger launch apertures there is potential for significant improvement with AO correction and less of a gain for smaller launch apertures where the diffractive effects dominate. Adaptive Optics can increase the mean received intensity and reduce the variance.

Larger launch beams result in smaller receiver-plane beam sizes due to reduced diffraction. This becomes even more pronounced after AO correction, which mitigates the atmospheric induced beam wander. For larger apertures, additional gains are made by correcting for higher-order modes (beyond tip/tilt) which will also reduce the short-term beam size. In this particular case, there is little gain by using an laser guide star (LGS); AO corrected using the downlink beam provides nearly optimal performance despite the point-ahead angle in terms of beam size.

The received intensity variance follows a similar trend, however, it is more sensitive to the residual beam motion and hence there are still significant gains to be made by using an LGS to mitigate the point-ahead angle. 'AO_PA' makes very little difference to the intensity variance when compared to small launch apertures. However, this still enables a higher received intensity, albeit with similar expected variance as a conventional smaller launch aperture.

For launch apertures of size $T_{R_x} < 0.05$m AO offers no performance advantage over tip/tilt correction. 'AO_PA' and 'LGS_PA' reach optimal performance for $T_{R_x} \approx 0.1$. Above these sizes, AO corrected receiver plane beam size is reduced and therefore residual tip/tilt (due to the point-ahead angle) becomes more important.

Figure 5 shows the probability of fade and expected BER for three example launch beam radii; 2 cm (left column) 10 cm (centre column) and 20 cm (right column).

As above, we can confirm that using tip/tilt correction provides nearly optimal performance for small launch apertures. For a 10 cm launch radius the tip/tilt correction results in a similar probability of fade as an uncorrected beam on a small (2 cm) launch aperture. AO can be seen to reduce the BER for a given signal-to-noise ratio, however, as can be seen in Fig. 4 (central panel), the received intensity is also increased, leading to a higher signal to noise ratio and therefore reducing the BER further. Using full AO correction will reduce the fade and BER in all cases except at very low signal-to-noise ratio.

For full AO and 'LGS_PA', minimal intensity variance is found with launch beam radii of 10 cm.

7.2. Launch beam shape

Due to the central obscuration on larger launch apertures it may not be possible to launch a Gaussian beam. Here we compare the propagation metrics for a Gaussian launch and a Bessel-Gaussian beam (Fig. 6). It is noted that the receiver plane beam shape for a Bessel-Gauss launch beam shape is also not Gaussian but actually has significant ringing in the long-exposure image.

It is difficult to compare the two launch geometries directly as the launch beam radius is defined as $1/e^2$ radius for a Gaussian beam but the radius of the full launch aperture is used for the Bessel-Gauss beam. However, it can be seen the metrics for comparable beam launch sizes are similar. This demonstrates that a Bessel-Gauss beam profile is a good candidate to enable large launch apertures where a secondary obscuration is present, without loss of performance.

7.3. LEO and GEO

Figure 7 shows the beam metrics for an uplink beam to LEO and GEO, both at 30 degrees elevation angle and both through the weak turbulence profile. The weak turbulence plots are repeated from Fig. 6 but the axis range has been modified for ease of comparison.

As expected the longer propagation distance leads to a significantly increased beam size at the receiver plane and hence a lower mean received intensity. However the uncorrected intensity variance is very similar for LEO and GEO links. This is because the larger absolute beam wander is balanced by the larger spatial coherence length of the scintillation pattern.
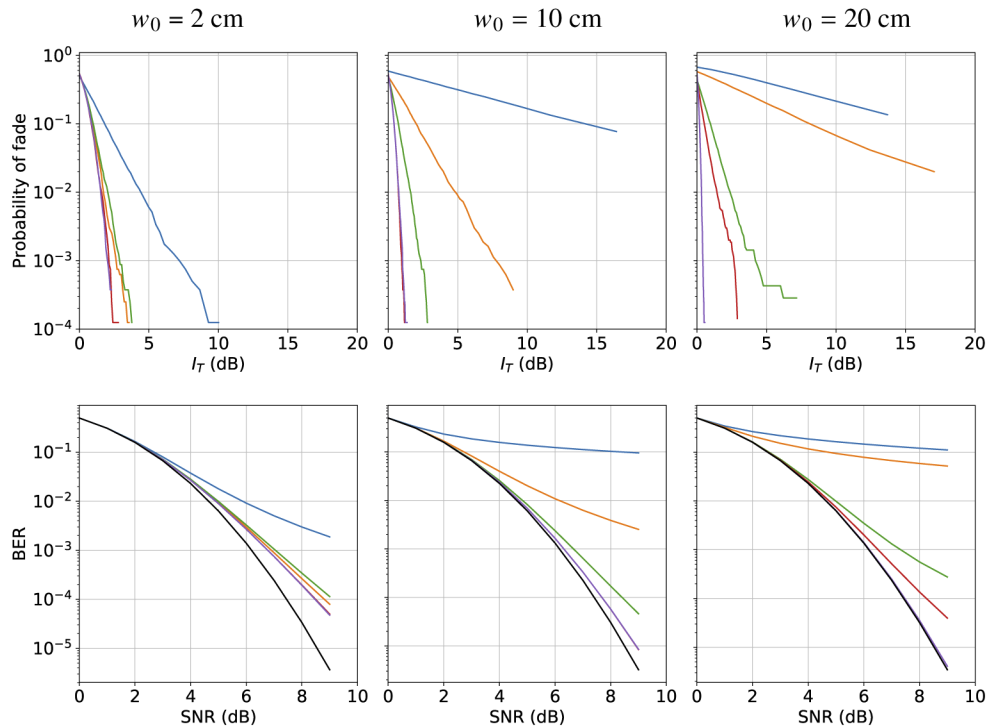
Fig. 5. Probability of fade (top row) and BER (bottom row) for various various adaptive mitigation for a 2 cm (left column) 10 cm (centre column) and 20 cm (right column) Gaussian launch beam radius and 1550 nm wavelength at 30 degrees elevation angle. The solid line on the BER plots show the 'free-space' link without any turbulence. The colour indicates the AO mode; blue is uncorrected; yellow is 'TT_PA'; green is 'AO_PA'; red is 'LGS_PA'; and purple is perfect 'AO'. AO reduces the probability of fade and increases the received intensity, reducing the BER.

For GEO, due to the smaller point-ahead angle, it can be seen that 'AO_PA', even with the point-ahead angle, can provide almost optimal correction for $1/e^2$ launch beam radius up to ~0.2 m and LGS correction can extend that range.

7.4. Ground layer turbulence strength

Table 4 shows the integrated turbulence parameters for the strong turbulence profile at 30 degree elevation. Figure 8 shows the effect of increasing the ground layer strength of the Hufnagel-Valley profile by an order of magnitude (ie weak turbulence profile to strong turbulence profile) for an uplink to LEO. This stronger profile is more consistent with daytime operations where the ground layer turbulence tends to be much stronger due to the solar heating of the ground. The weak turbulence plots are repeated from Fig. 6 for ease of comparison.

The uncorrected beam size at the receiver plane is significantly larger due to the additional turbulence induced beam wander. This leads to a lower received intensity and therefore lower signal-to-noise ratio. The received intensity variance is higher due to a higher beam motion and scintillation.

Unlike the weak turbulence case, tip/tilt only and 'AO_PA' only provide marginal performance improvements. In strong turbulence conditions, 'LGS_PA' is required to reach optimal performance but launch apertures should be limited to approximately 10 cm in radius.
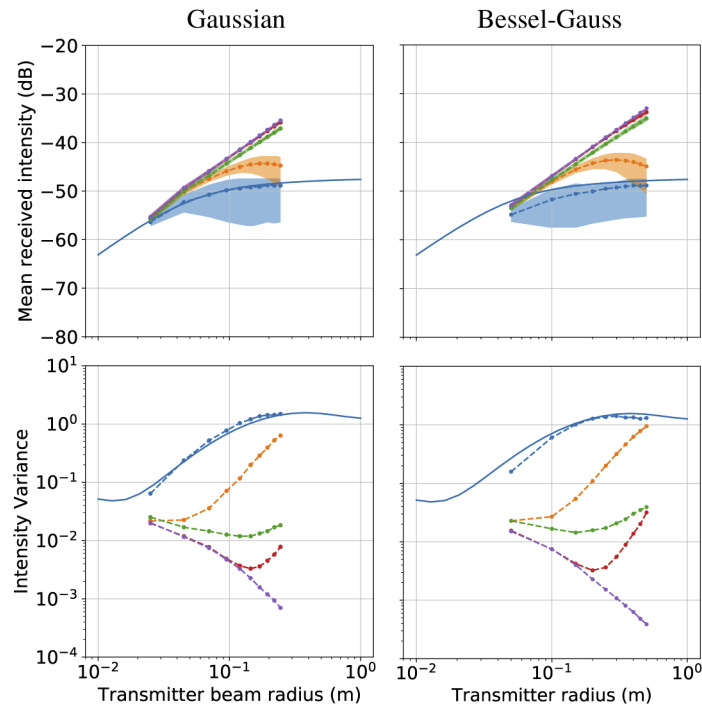
Fig. 6. Expected beam parameters with various correction techniques for an uplink optical propagation to LEO at 30 degrees elevation and at 1550 nm for a Gaussian (left column) and a Bessel-Gauss (right column) launch beamshape. From top to bottom, the rows show the fractional received intensity and intensity variance. The solid lines indicate the theoretical values for an uncorrected, collimated, Gaussian beam, however the data are for a Bessel-Gauss beam and are therefore not expected to match the theory - it is shown only for easy comparison. For the mean received intensity, the coloured region indicates the inter-quartile range of the distribution. The colour indicates the AO mode; blue is uncorrected; yellow is 'TT_PA'; green is 'AO_PA'; red is 'LGS_PA'; and purple is perfect 'AO'.

Table 4. Integrated atmospheric parameters for the strong turbulence profile at 30 degree elevation.

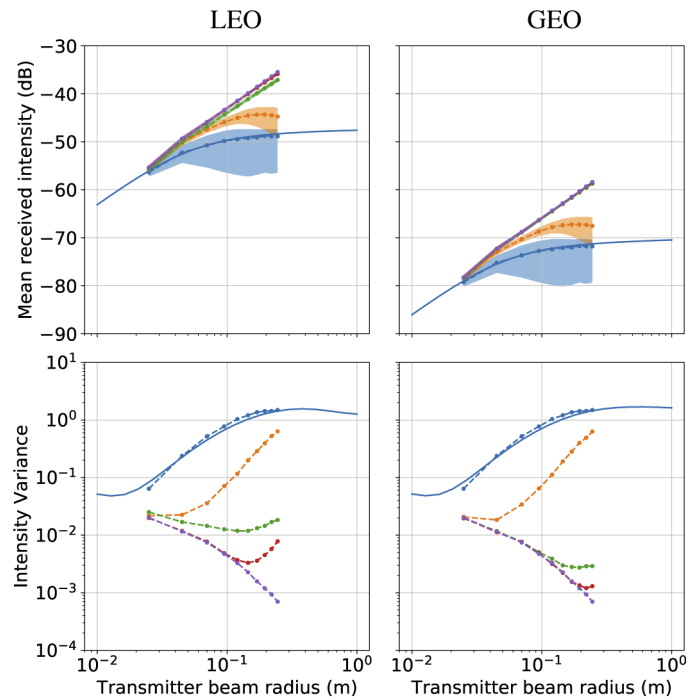| Optical turbulence parameters	Strong turbulence 30 degrees	
λ (nm)	500	1550
Coherence length r_0 (cm)	1.0	3.7
Isoplanatic angle θ_0 (μ rad)	2.20	8.56
Downlink Rytov variance σ_R^2	2.71	0.73

Fig. 7. Expected beam parameters with various correction techniques for an uplink optical propagation to LEO (left) and GEO (right) for Gaussian beam shapes and a 5cm (LEO) or 25cm (GEO) receiver, at 1550 nm and 30 degrees elevation. From top to bottom, the rows show the fractional received intensity and intensity variance. The solid lines indicate the theoretical values for an uncorrected, collimated, Gaussian beam. For the mean received intensity, the coloured region indicates the inter-quartile range of the distribution. The colour indicates the AO mode; blue is uncorrected; yellow is 'TT_PA'; green is 'AO_PA'; red is 'LGS_PA'; and purple is perfect 'AO'.

7.5. Wavelength

Table 5 shows the integrated turbulence parameters for the weak turbulence profile for 850, 1064 and 1550 nm wavelengths at 30 degree elevation angle. Figure 9 shows the beam metrics for a LEO uplink beam through weak turbulence at 30 degree elevation for wavelengths of 850, 1064 and 1550 nm. The 1550 nm plots are repeated from Fig. 6 for ease of comparison.

Table 5. Integrated atmospheric parameters for the weak turbulence profile at 30 degree elevation.

Optical turbulence parameters	Wavelength (nm)		
	850	1064	1550
Coherence length r_0 (cm)	6.2	8.1	12.8
Isoplanatic angle θ_0 (μ rad)	4.47	5.85	9.19
Downlink Rytov variance σ_R^2	0.43	0.33	0.21

Shorter wavelengths are more disrupted by optical turbulence than longer wavelengths. This will lead to increased beam wander and hence a larger beam size in the receiver plane. However, due to diffraction longer wavelengths also result in a larger beam size. Therefore there is a balance between increased apparent turbulence strength at shorter wavelengths and diffraction at longer
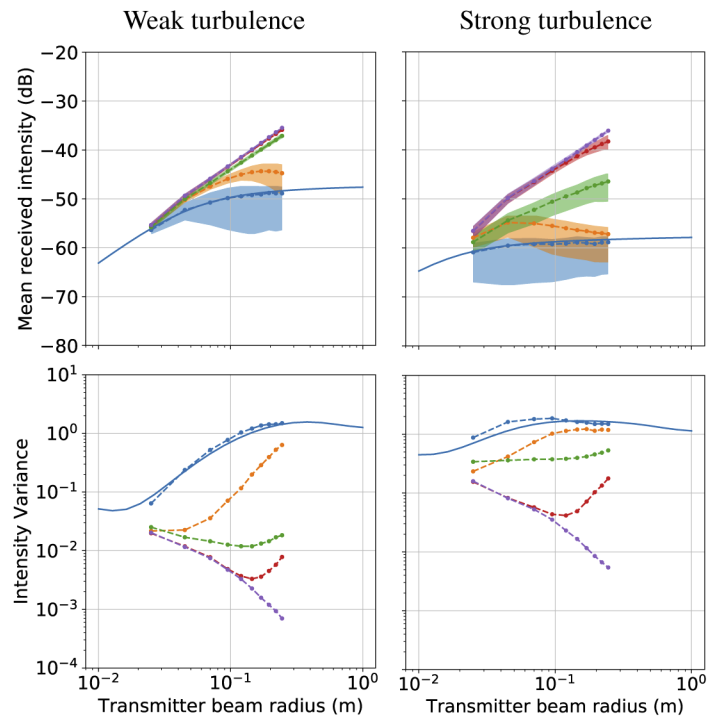
Fig. 8. Expected beam parameters with various correction techniques for an uplink optical propagation to LEO for weak ground layer profile (left) and strong ground layer profile (right) at 1550 nm and 30 degrees elevation. From top to bottom, the rows show the fractional received intensity and intensity variance. For the mean received intensity, the coloured region indicates the inter-quartile range of the distribution. The colour indicates the AO mode; blue is uncorrected; yellow is 'TT_PA'; green is 'AO_PA'; red is 'LGS_PA'; and purple is perfect 'AO'.

wavelengths with the result determined by the atmospheric conditions at the time. Figure 9 shows that, in this case, the uncorrected received mean intensity and variance are both approximately the same for all wavelengths.

7.6. Elevation angle

The elevation angle significantly influences the propagation of light through the atmosphere through four effects:

i) Lower elevation angles increase the propagation distance between turbulent zones and to the receiver plane, increasing the scintillation.

ii) Lower elevation angle also increases the area of the beam projected onto the turbulent layers due to the angular offset between the beam direction and the horizontal turbulent layer - the projected beam shape is an oval rather than a circle as at zenith. This increased beam size at low elevation angles also increases the apparent strength of the layer - increasing the turbulent effects.

iii) the increased propagation distance leads to greater diffractive beam spread which acts to increase the apparent strength of the turbulence (as with ii) but also means that the downlink and uplink are not reciprocal. In the case that the downlink beam is used as a
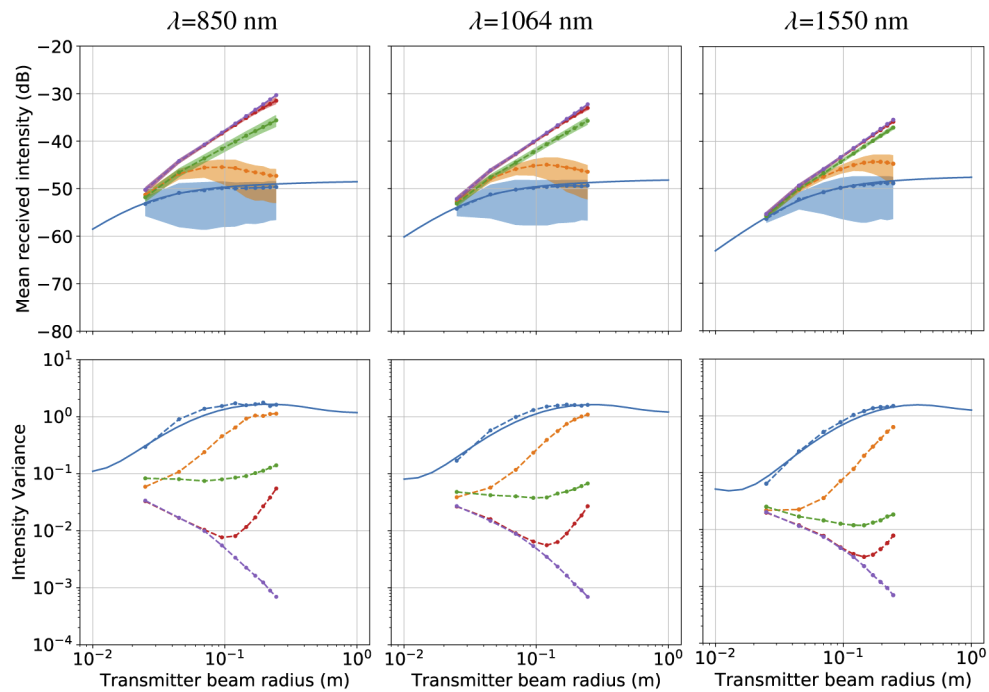
Fig. 9. Expected beam parameters with various correction techniques for an uplink optical propagation to LEO for various wavelengths (850, 1064 and 1550 nm - columns left to right) at 30 degree elevation angle. From top to bottom, the rows show the fractional received intensity and intensity variance. The solid lines indicate the theoretical values for an uncorrected, collimated, Gaussian beam. For the mean received intensity, the coloured region indicates the inter-quartile range of the distribution. The colour indicates the AO mode; blue is uncorrected; yellow is 'TT_PA'; green is 'AO_PA'; red is 'LGS_PA'; and purple is perfect 'AO'.

probe for AO correction, either full or tip/tilt, these signals will be less correlated with the uplink - reducing the AO performance. This is also true at zenith but is amplified at lower elevation angles.

iv) For AO correction the increased propagation distance combined with the point-ahead angle leads to a greater absolute separation between down and uplink beam paths on the turbulence layers. This increased separation leads to a lower correlation of the wavefront, effectively reducing the performance of the AO correction.

Table 6 shows the integrated turbulence parameters for the weak turbulence profile for 1550 nm wavelengths at 10, 30 and 90 degree elevation angle. Figure 10 shows the metrics for the atmospheric propagation for weak turbulence to LEO at elevation angles of 10, 30 and 90 degrees. The 30 degree elevation angle plots are repeated from Fig. 6 for ease of comparison.

The expected receiver beam size is significantly larger for lower elevation angles, this corresponds to a lower mean received intensity and hence lower signal-to-noise ratio. Lower elevation angles also result in higher intensity variance, increasing the probability of signal fade. This trend is also true for the various turbulence mitigation schemes until we reach very low elevation angles. At 10 degrees elevation the tip/tilt only correction ('TT_PA') results in a smaller beam size and lower received intensity variance than full AO correction (using the downlink as the probe, 'AO_PA'). This is due to the effect of (iii and iv) listed above. As the downlink and
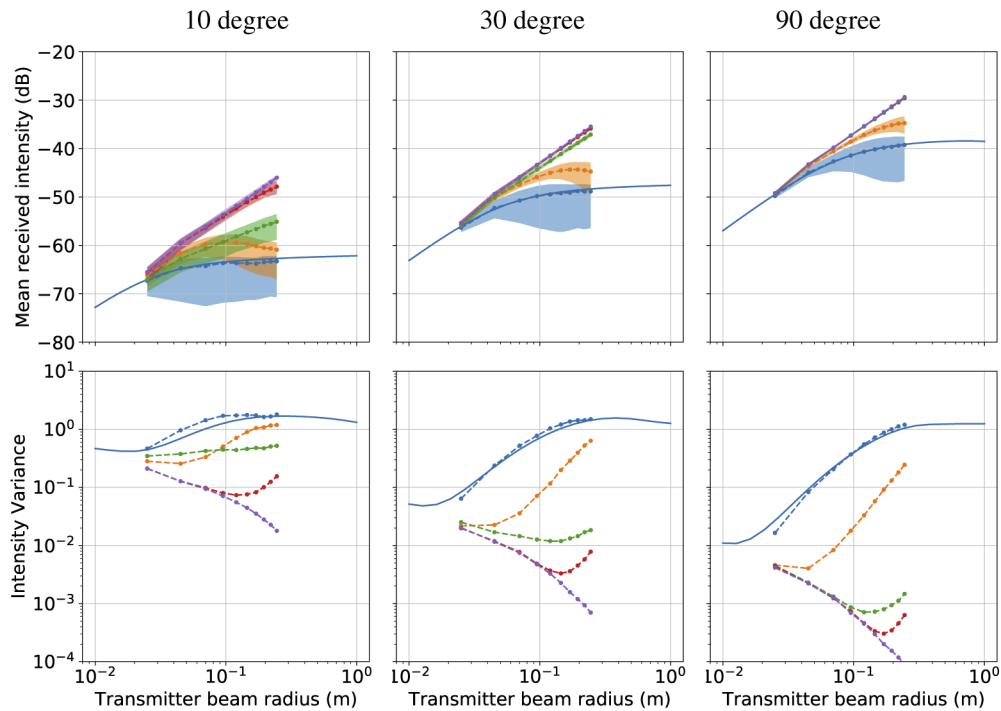
Fig. 10. Expected beam parameters with various correction techniques for an uplink optical propagation to LEO at 10 degree (left), 30 degree (centre) and 90 degree (right) elevation for Gaussian launch beam at 1550 nm. From top to bottom, the rows show the fractional received intensity and intensity variance. The solid lines indicate the theoretical values for an uncorrected, collimated, Gaussian beam. For the mean received intensity, the coloured region indicates the inter-quartile range of the distribution. The colour indicates the AO mode; blue is uncorrected; yellow is 'TT_PA'; green is 'AO_PA'; red is 'LGS_PA'; and purple is perfect 'AO'.

Table 6. Integrated atmospheric parameters for the weak turbulence profile for a wavelength of 1550 nm.

Optical turbulence parameters	Elevation angle (degrees)		
	10	30	90
Coherence length r_0 (cm)	6.8	12.8	19.3
Isoplanatic angle θ_0 (μ rad)	1.69	9.19	27.86
Downlink Rytov variance σ_R^2	1.48	0.21	0.06

uplink paths are no longer reciprocal - due to the diffractive effects over the elongated path length at low elevation angles - the higher order modes are uncorrelated. This decorrelation effectively means that trying to correct for high-order modes makes the correction worse. This is not the case for tip/tilt correction which is correlated over a larger area.

We can also see that at low elevation angles even perfect AO correction is significantly worse (lower mean received intensity and higher variance) than at higher elevation angles. This is due to the fact that the up and downlink paths are not reciprocal and forms a limit to AO performance for uplink propagation.

8. Discussion

We show that AO always improves the link with a higher received intensity (higher signal-to-noise ratio) and less variance (lower fade probability) in the receiver plane. The magnitude of the improvement is dependent upon the parameters described above. This improvement comes from realising the potential of larger launch apertures which result in smaller geometric divergence. However, this potential can only be realised with the use of AO otherwise the turbulence induced beam-wander and scintillation will dominate and degrade performance relative to a small launch aperture.

Perfect AO correction does not mean perfect correction. Perfect AO still uses a hypothetical downlink beam at the point-ahead angle and so does not include the geometric divergence of the uplink beam, meaning that the beams are not reciprocal, and therefore there is still residual intensity variance and a non-optimal mean received intensity. This case is presented as a best case scenario to show the full potential of AO for uplink correction.

We have shown that tip/tilt correction is sufficient for smaller launch apertures (*i.e.* less than 5 cm) to reach optimal (perfect AO) performance.

AO on larger launch apertures enables greater performance gains. By mitigating the turbulence the received intensity variance is reduced, reducing the probability of fade, and the beam spread is dominated by geometric diffraction and so larger launch apertures lead to smaller receiver-plane beam sizes and hence higher signal-to-noise ratios.

LGS AO outperforms full AO as the higher-order modes are not affected by the point-ahead angle. Both have a minima of fade probability for launch apertures of approximately 10cm in beam radius. However the mean received intensity and hence signal increases with increasing launch aperture.

We also show that the performance is strongly dependent on the vertical profile of the atmospheric turbulence. For example, if all of the turbulence was at the ground, the point-ahead angle would have no effect and AO, LGS AO and perfect AO would all have the same result.

These larger launch beams are difficult to support in reality due to larger telescopes generally having a central obscuration. There have been suggestions of using a Bessel-Gauss beam rather than a pure Gaussian beam shape. There are difficulties in comparing different launch beam shapes. However, we have shown that a Bessel-Gauss beam has similar performance to a Gaussian beam and could be a viable option when using launch telescopes with a secondary obscuration.

The performance of the system is very sensitive to the turbulence profile. By changing the ground turbulence strength we show a very significant change in link metrics. This means that we can expect different performance for the system during the daytime and the night-time. We see that significant performance gains are expected with full AO for weak turbulence, but for stronger turbulence an LGS at the point-ahead angle is needed.

In the case of GEO links the increased propagation distance with respect to LEO links means that the receiver plane beam size is considerably larger and hence a lower intensity is received. However, the uncorrected and Tip/Tilt corrected received intensity variance is similar for the two propagation distances, with full AO and LGS AO leading to lower variance for GEO links due to the smaller point-ahead angle. The minima intensity variance for the AO and LGS AO for GEO is approximately 20 cm, larger than for LEO, resulting in a lower optimal intensity variance.

Links using shorter wavelengths are more adversely affected by turbulence, and therefore have a lower received intensity. However, the received intensity only has a weak dependence on wavelength as shorter wavelengths are more susceptible to turbulence induced beam spread whereas longer wavelengths have a larger diffractive beam spread. This means that shorter wavelengths have the potential for a higher signal-to-noise ratio if the turbulence is corrected.

As expected the performance of the link is worse at lower elevation angles where the longer propagation distances and the larger beam size on the turbulent layers both lead to a larger beam size, lower intensity and higher intensity variance in the receiver plane.

Some interesting cases occur in strong turbulence conditions (for example, day-time, low elevation angles or shorter wavelengths). In these cases the point-ahead angle means that the downlink and uplink beam are no longer correlated for high order modes, and simple Tip/tilt correction outperforms downlink AO correction, particularly for smaller launch telescope sizes.

Stronger turbulence conditions also bring practical difficulties that are not considered in this study. For the results demonstrated here to be realised in practice, certain advancements in the field of FSOC are AO are required. The Shack-Hartmann Wavefront Sensor, the most commonly used wavefront sensing device in AO, has been shown to perform poorly in "strong turbulence" conditions due to so called "branch cuts" in the phase function [23–25]. Improved wavefront reconstruction techniques have been suggested which mitigate this effect [26–28]. Further, dedicated "strong wavefront sensor" devices have been proposed, such as interferometric solutions which extend AO operation into strong atmospheric conditions [8,29–31]. The fast changing turbulence in "strong" conditions requires a fast AO control loop bandwidth in comparison to astronomical AO systems. Recent demonstrations have been made with long horizontal links that show that AO is possible in these conditions, provided an adequately fast infra-red wavefront sensor detector is used with an optimised AO real-time control system [2,32,33]. Lastly, the use of a LGS is assumed here to be a possibility in daytime FSOC, which is yet to be proven in practice. The main challenge here with respect to existing astronomical LGS AO systems is the smaller return flux associated with a smaller receiver aperture. This can be mitigated by creating a brighter LGS beacon with developments in this topic ongoing. More powerful laser sources are becoming available and other novel techniques to improve LGS efficiency, such as "Chirping", are under investigation [34,35]. It is currently assumed that LGS cannot provide tip/tilt information, but studies are ongoing to overcome even this limitation [36], potentially enabling even the "perfect AO" scenario considered here.

9. Conclusion

We have developed a laser propagation Monte-Carlo simulation and used it to test various AO mitigation scenarios for laser propagation through the Earth's turbulent atmosphere between the ground and space and used this to explore the parameters open to designers of ground stations for FSOC.

This study uses an idealised model of AO and therefore demonstrates the potential of AO for applications such as FSOC. However, that potential is currently difficult to realise with research into the effects of strong and fast turbulence and strong scintillation required. In addition, this study uses a standard atmospheric model. There is a lack of atmospheric data for realistic modelling of the optical link, particularly in non-astronomical observatories and at low elevation angles. Further studies include linking realistic AO models with new atmospheric data in difficult conditions in order to assess realistic optical links.

The test conditions included typical scenarios for orbiting objects in LEO and GEO orbits. We tested five different correction techniques; no AO, tip/tilt AO - using a downlink beam as the atmospheric probe, full AO - using a downlink beam as the atmospheric probe, LGS AO - using a laser guide star at the point-ahead angle for the high-order modes and tip/tilt/focus from the downlink, and perfect AO - in order to assess the ultimate performance of the link. We considered transmitter diameter, wavelength, launch beam geometry, turbulence strength, elevation angle to links at LEO and GEO.

In all cases, AO was shown to increase the mean received intensity and reduce the intensity variance. A minimum of received intensity variance was found for a Gaussian launch beam radius, w_0, of approximately 10 cm, depending on conditions. We also show that similar results can be expected from a Bessel-Gauss beam, demonstrating that the required large launch apertures, where a secondary obscuration is present, can be used without loss of performance.

We also show the expected improvement in probability of fade and Bit-Error-Rate. We see that AO to pre-compensate an uplink beam will reduce the fade and BER in all cases except for small launch apertures and at very low signal-to-noise ratios. Therefore the benefit of AO is to use larger apertures to increase the received signal-to-noise ratio.

The data used to generate the figures in this manuscript are available on reasonable request to the author.

Disclosures. The authors declare no conflicts of interest.

References

1. V. W. S. Chan, "Free-space optical communications," J. Lightwave Technol. **24**(12), 4750–4762 (2006).
2. R. Mata Calvo, J. Poliak, J. Surof, A. Reeves, M. Richerzhagen, H. F. Kelemu, R. Barrios, C. Carrizo, R. Wolf, F. Rein, A. Dochhan, K. Saucke, and W. Luetke, "Optical technologies for very high throughput satellite communications," in *Free. Laser Commun. XXXI*, vol. 10910 H. Hemmati and D. M. Boroson, eds. (SPIE, 2019), p. 31.
3. C. Erven, C. Couteau, R. Laflamme, and G. Weihs, "Entangled quantum key distribution over two free-space optical links," Opt. Express **16**(21), 16840–16853 (2008).
4. M. Polnik, L. Mazzarella, M. Di Carlo, D. K. Oi, A. Riccardi, and A. Arulselvan, "Scheduling of space to ground quantum key distribution," EPJ Quantum Technol. **7**(1), 3 (2020).
5. A. C. Motlagh, V. Ahmadi, Z. Ghassemlooy, and K. Abedi, "The effect of atmospheric turbulence on the performance of the free space optical communications," in *Proc. 6th Int. Symp. Commun. Syst. Networks Digit. Signal Process. CSNDSP 08*, (2008), pp. 540–543.
6. R. K. Tyson, "Adaptive optics and ground-to-space laser communications," Appl. Opt. **35**(19), 3640 (1996).
7. C. Petit, N. Védrenne, M.-T. Velluet, V. Michau, G. Artaud, E. Samain, M. Toyoshima, C. Petit, N. Védrenne, M.-T. Velluet, V. Michau, G. Artaud, E. Samain, and M. Toyoshima, "Investigation of adaptive optics performance through propagation channel characterization with the Small Optical TrAnsponder SOTA," Opt. TrAnsponder SOTA. Opt. Eng. **55**(11), 111611 (2016).
8. M. Knapek, "Adaptive Optics for the Mitigation of Atmospheric Effects in Laser Satellite-To-Ground Communications," Ph.D. thesis (2010).
9. N. Martínez Rey, L. F. Rodríguez Ramos, and Z. Sodnik, "Uplink wavefront corrector system: from paper to reality," Opt. Express **28**(5), 5886 (2020).
10. A. Alonso, M. Reyes, and Z. Sodnik, "Performance of satellite-to-ground communications link between ARTEMIS and the Optical Ground Station," in *Opt. Atmos. Propag. Adapt. Syst. VII*, vol. 5572 J. D. Gonglewski and K. Stein, eds. (SPIE, 2004), p. 372.
11. T. Plank, E. Leitgeb, P. Pezzei, and Z. Ghassemlooy, "Wavelength-selection for high data rate Free Space Optics (FSO) in next generation wireless communications," in *2012 17th Eur. Conf. Netw. Opt. Commun. NOC 2012, 7th Conf. Opt. Cabling Infrastructure, OC I 2012*, (2012).
12. N. Martínez, L. F. Rodríguez-Ramos, and Z. Sodnik, "Toward the uplink correction: application of adaptive optics techniques on free-space optical communications through the atmosphere," Opt. Eng. **57**(07), 1 (2018).
13. S. K. Liao, W. Q. Cai, W. Y. Liu, L. Zhang, Y. Li, J. G. Ren, J. Yin, Q. Shen, Y. Cao, Z. P. Li, F. Z. Li, X. W. Chen, L. H. Sun, J. J. Jia, J. C. Wu, X. J. Jiang, J. F. Wang, Y. M. Huang, Q. Wang, Y. L. Zhou, L. Deng, T. Xi, L. Ma, T. Hu, Q. Zhang, Y. A. Chen, N. L. Liu, X. B. Wang, Z. C. Zhu, C. Y. Lu, R. Shu, C. Z. Peng, J. Y. Wang, and J. W. Pan, "Satellite-to-ground quantum key distribution," Nature **549**(7670), 43–47 (2017).
14. M. J. Townson, O. J. D. Farley, G. Orban de Xivry, J. Osborn, and A. P. Reeves, "AOtools: a Python package for adaptive optics modelling and analysis," Opt. Express **27**(22), 31316 (2019).
15. J. D. Schmidt, *Numerical Simulation of Optical Wave Propagation with Examples in MATLAB* (SPIE, 2010).
16. J. Osborn, T. Butterley, S. Perera, D. Fohring, and R. Wilson, "Observations of the dynamic turbulence above La Palma using Stereo-SCIDAR," in *Adapt. Opt. Extrem. Large Telesc. 4–Conference Proc.*, vol. 1 (2015).
17. J. Osborn, R. W. Wilson, M. Sarazin, T. Butterley, A. Chacón, F. Derie, O. J. D. Farley, X. Haubois, D. Laidlaw, M. LeLouarn, E. Masciadri, J. Milli, J. Navarrete, and M. J. Townson, "Optical turbulence profiling with Stereo-SCIDAR for VLT and ELT," Mon. Not. R. Astron. Soc. **478**(1), 825–834 (2018).
18. O. J. D. Farley, J. Osborn, T. Morris, M. Sarazin, T. Butterley, M. J. Townson, P. Jia, and R. W. Wilson, "Representative optical turbulence profiles for ESO Paranal by hierarchical clustering," Mon. Not. R. Astron. Soc. **481**(3), 4030–4037 (2018).
19. L. C. Andrews, R. L. Phillips, D. Wayne, T. Leclerc, P. Sauer, R. Crabbs, and J. Kiriazes, "Near-ground vertical profile of refractive-index fluctuations," in *Atmos. Propag. VI*, vol. 7324 L. M. Wasiczko Thomas and G. C. Gilbreath, eds. (SPIE, 2009), p. 732402.
20. L. C. Andrews and R. L. Phillips, *Laser Beam Propagation through Random Media* (SPIE, 2009).

21. T. Fusco, J.-M. Conan, V. Michau, L. M. Mugnier, and G. Rousset, "Efficient phase estimation for large-field-of-view adaptive optics," Opt. Lett. **24**(21), 1472 (1999).

22. M. Beason, S. Gladysz, and L. Andrews, "Comparison of probability density functions for aperture-averaged irradiance fluctuations of a Gaussian beam with beam wander," Appl. Opt. **59**(20), 6102 (2020).

23. D. L. Fried and J. L. Vaughn, "Branch cuts in the phase function," Appl. Opt. **31**(15), 2865–2882 (1992).

24. D. L. Fried, "Branch point problem in adaptive optics," J. Opt. Soc. Am. A **15**(10), 2759–2768 (1998).

25. J. D. Barchers, D. L. Fried, and D. J. Link, "Evaluation of the performance of hartmann sensors in strong scintillation," Appl. Opt. **41**(6), 1012–1021 (2002).

26. D. L. Fried, "Adaptive optics wave function reconstruction and phase unwrapping when branch points are present," Opt. Commun. **200**(1-6), 43–72 (2001).

27. T. A. Rhoadarmer, J. D. Barchers, and E. J. Spillar, "Complex field reconstruction using gradient and intensity measurements from a shack-hartmann wave front sensor," in *Adaptive Optics Systems and Technology II*, vol. 4494 (International Society for Optics and Photonics, 2002), pp. 233–244.

28. K. Murphy, R. Mackey, and C. Dainty, "Branch point detection and correction using the branch point potential method," in *Atmospheric Propagation V*, vol. 6951 (International Society for Optics and Photonics, 2008), p. 695105.

29. J. Notaras and C. Paterson, "Point-diffraction interferometer for atmospheric adaptive optics in strong scintillation," Opt. Commun. **281**(3), 360–367 (2008).

30. J. D. Barchers, D. L. Fried, D. J. Link, G. A. Tyler, W. Moretti, T. J. Brennan, and R. Q. Fugate, "Performance of wavefront sensors in strong scintillation," in *Adaptive Optical System Technologies II*, vol. 4839 (International Society for Optics and Photonics, 2003), pp. 217–227.

31. C. E. Carrizo, R. M. Calvo, and A. Belmonte, "Intensity-based adaptive optics with sequential optimization for laser communications," Opt. Express **26**(13), 16044–16053 (2018).

32. R. Saathof, R. den Breeje, W. Klop, N. Doelman, T. Moens, M. Gruber, T. Russchenberg, F. Pettazzi, J. Human, R. M. Calvo, J. Poliak, R. Barrios, M. Richerzhagen, and I. Ferrario, "Adaptive optics pre-correction for optical feeder links: breadboard performance," in *International Conference on Space Optics — ICSO 2018*, vol. 11180 Z. Sodnik, N. Karafolas, and B. Cugny, eds., International Society for Optics and Photonics (SPIE, 2019), pp. 897–905.

33. A. Montmerle-Bonnefois, C. Petit, C. Lim, J.-F. Sauvage, S. Meimon, P. Perrault, F. Mendez, B. Fleury, J. Montri, J.-M. Conan, V. Michau, N. Védrenne, Z. Sodnik, and C. Voland, "Adaptive optics precompensation of a geo feeder link : the feedelio experiment," in *Laser Congress 2019 (ASSL, LAC, LS&C)*, (Optical Society of America, 2019), p. LTh1B.3.

34. R. L. Johnson, M. O. Byrd, K. Wyman, and L. Kann, "Recent progress in sodium beacon development," in *Adaptive Optics Systems VII*, vol. 11448 L. Schreiber, D. Schmidt, and E. Vernet, eds., International Society for Optics and Photonics (SPIE, 2020).

35. F. P. Bustos, R. Holzlöhner, S. Rochester, D. B. Calia, J. Hellemeier, and D. Budker, "Frequency chirped continuous-wave sodium laser guide stars: modeling and optimization," J. Opt. Soc. Am. B **37**(4), 1208–1218 (2020).

36. R. Mata-Calvo, D. B. Calia, R. Barrios, M. Centrone, D. Giggenbach, G. Lombardi, P. Becker, and I. Zayer, "Laser guide stars for optical free-space communications," in *Free-Space Laser Communication and Atmospheric Propagation XXIX*, vol. 10096 H. Hemmati and D. M. Boroson, eds., International Society for Optics and Photonics (SPIE, 2017), pp. 188–199.

37. S. Van der walt, S. C. Colbert, and V. Gaël, "The NumPy array: a structure for efficient numerical computation," Comput. Sci. Eng. **13**(2), 22–30 (2011).

38. P. Virtanen, R. Gommers, T. E. Oliphant, M. Haberland, T. Reddy, D. Cournapeau, E. Burovski, P. Peterson, W. Weckesser, J. Bright, S. J. van der Walt, M. Brett, J. Wilson, K. J. Millman, N. Mayorov, A. R. Nelson, E. Jones, R. Kern, E. Larson, C. J. Carey, I. Polat, Y. Feng, E. W. Moore, J. VanderPlas, D. Laxalde, J. Perktold, R. Cimrman, I. Henriksen, E. A. Quintero, C. R. Harris, A. M. Archibald, A. H. Ribeiro, F. Pedregosa, P. van Mulbregt, A. Vijaykumar, A. P. Bardelli, A. Rothberg, A. Hilboll, A. Kloeckner, A. Scopatz, A. Lee, A. Rokem, C. N. Woods, C. Fulton, C. Masson, C. Häggström, C. Fitzgerald, D. A. Nicholson, D. R. Hagen, D. V. Pasechnik, E. Olivetti, E. Martin, E. Wieser, F. Silva, F. Lenders, F. Wilhelm, G. Young, G. A. Price, G. L. Ingold, G. E. Allen, G. R. Lee, H. Audren, I. Probst, J. P. Dietrich, J. Silterra, J. T. Webber, J. Slavič, J. Nothman, J. Buchner, J. Kulick, J. L. Schönberger, J. V. de Miranda Cardoso, J. Reimer, J. Harrington, J. L. C. Rodríguez, J. Nunez-Iglesias, J. Kuczynski, K. Tritz, M. Thoma, M. Newville, M. Kümmerer, M. Bolingbroke, M. Tartre, M. Pak, N. J. Smith, N. Nowaczyk, N. Shebanov, O. Pavlyk, P. A. Brodtkorb, P. Lee, R. T. McGibbon, R. Feldbauer, S. Lewis, S. Tygier, S. Sievert, S. Vigna, S. Peterson, S. More, T. Pudlik, T. Oshima, T. J. Pingel, T. P. Robitaille, T. Spura, T. R. Jones, T. Cera, T. Leslie, T. Zito, T. Krauss, U. Upadhyay, Y. O. Halchenko, and Y. Vázquez-Baeza, "SciPy 1.0: fundamental algorithms for scientific computing in Python," Nat. Methods **17**(3), 261–272 (2020).

39. J. D. Hunter, "Matplotlib: A 2D graphics environment," Comput. Sci. Eng. **9**(3), 90–95 (2007).